nature materials

ARTICLES

https://doi.org/10.1038/s41563-020-00831-1

Printable two-dimensional superconducting monolayers

Jing Li[1,2,7], Peng Song[1,7], Jinpei Zhao[3,7], Kristina Vaklinova[2,7], Xiaoxu Zhao[4,7], Zejun Li[1], Zhizhan Qiu[1], Zihao Wang[5], Li Lin[5], Meng Zhao[6], Tun Seng Herng[4], Yuxin Zuo[4], Win Jonhson[4], Wei Yu[1], Xiao Hai[1], Pin Lyu[1], Haomin Xu[1], Huimin Yang[1], Cheng Chen[1], Stephen J. Pennycook[4], Jun Ding[4], Jinghua Teng[6], A. H. Castro Neto[2,3,4], Kostya S. Novoselov[2,4,5]✉ and Jiong Lu[1,2]✉

Two-dimensional superconductor (2DSC) monolayers with non-centrosymmetry exhibit unconventional Ising pair superconductivity and an enhanced upper critical field beyond the Pauli paramagnetic limit, driving intense research interest. However, they are often susceptible to structural disorder and environmental oxidation, which destroy electronic coherence and provide technical challenges in the creation of artificial van der Waals heterostructures (vdWHs) for devices. Herein, we report a general and scalable synthesis of highly crystalline 2DSC monolayers via a mild electrochemical exfoliation method using flexible organic ammonium cations solvated with neutral solvent molecules as co-intercalants. Using $NbSe_2$ as a model system, we achieved a high yield (>75%) of large-sized single-crystal monolayers up to 300 μm. The as-fabricated, twisted $NbSe_2$ vdWHs demonstrate high stability, good interfacial properties and a critical current that is modulated by magnetic field when one flux quantum fits to an integer number of moiré cells. Additionally, formulated 2DSC inks can be exploited to fabricate wafer-scale 2D superconducting wire arrays and three-dimensional superconducting composites with desirable morphologies.

Two-dimensional (2D) transition metal dichalcogenide (TMD) superconductors provide a platform for the investigation of quantum physics and exotic superconductivity owing to their confined geometry with a strong spin–orbit coupling[1–5]. Van der Waals heterostructures (vdWHs) based on such crystals allow the creation of artificial, strongly correlated materials, with full control over the symmetry and the dimensionality of the resulting structures[6,7]. The exploration of these systems may lead to the discovery of atomically thin superconductors with exotic states and new superconducting mechanisms[8–12]. However, while the quality of highly crystalline two-dimensional superconductors (2DSCs) set them apart from conventional 2DSCs with granular and amorphous structures[13–15], the bottleneck in this field has been the lack of a general and facile approach for the production of high-quality atomic layers of 2DSCs in large quantities for practical applications[1]. Recently, advances in thin-film synthesis technologies have enabled the preparation of 2DSC TMD monolayers via different fabrication approaches, including mechanical exfoliation[10], molecular beam epitaxy (MBE)[8,11], chemical vapour deposition (CVD)[16–18] and chemical intercalation[19–23]. Unfortunately, none of these approaches offers simultaneous high crystallinity, high production yield, scalability of as-prepared flakes and ease of incorporation into the final devices, which severely hampers further advancement in this field. These constraints have motivated us to devise a general and versatile approach for the production of high-quality atomic layers of 2DSCs in large amounts for the fabrication of basic vdWHs and for potential use in quantum devices.

Solution-phase exfoliation of layered bulks into low-dimensional nanosheets offers competitive advantages in scalability and processability[19,20]. Small-sized lithium ion has been widely used to intercalate layered materials followed by good dispersion in polar solvents, resulting in a high yield of monolayer flakes[21,22,24,25]. To avoid the possible phase transition in TMDs arising from electron injection during the intercalation of lithium, the large-sized tetraheptyl ammonium cation was used as intercalant to prepare phase-pure few-layer semiconducting sheets[23]. However, increase of the cation size inevitably increases the intercalation barrier and thus reduces the intercalation and exfoliation rate of bulk crystals. In this regard, we developed a flexible co-intercalant of ammonium cations solvated with a large amount of neutral solvent molecules for the electrochemical exfoliation of 2DSC monolayer sheets. This strategy not only allows for sufficient intercalation of bulk crystals, but also notably reduces the excessive charging and structural damage of the layered hosts that arises from charged intercalants, which is crucial for exfoliation of high-quality and large-size 2DSC monolayers. The protective properties of the solvents and high quality of the 2DSC flakes enable easy fabrication of twisted vdWHs and wafer-scale printed film with a clean interface and new superconducting properties. The moiré pattern, formed at the interface between two $NbSe_2$ crystals, acts as an array of Josephson junctions, leading to oscillations in the critical current every time an integer number of flux quanta fits the moiré plaquette. Moreover, the printed $NbSe_2$ film exhibits an enhanced upper critical field, superconducting transition temperature and air stability, opening up a wide range of potential applications of 2D TMD superconductors beyond that of the monolayer.

Here, we demonstrate a universal method of electrochemical exfoliation of bulk TMDs using quaternary ammonium cations as

[1]Department of Chemistry, National University of Singapore, Singapore, Singapore. [2]Centre for Advanced 2D Materials and Graphene Research Centre, National University of Singapore, Singapore, Singapore. [3]Department of Physics, National University of Singapore, Singapore, Singapore. [4]Department of Materials Science & Engineering, National University of Singapore, Singapore, Singapore. [5]National Graphene Institute, University of Manchester, Manchester, UK. [6]Institute of Materials Research and Engineering, Agency for Science, Technology and Research (A*STAR), Singapore, Singapore. [7]These authors contributed equally: Jing Li, Peng Song, Jinpei Zhao, Kristina Vaklinova, Xiaoxu Zhao. ✉e-mail: kostya@nus.edu.sg; chmluj@nus.edu.sg

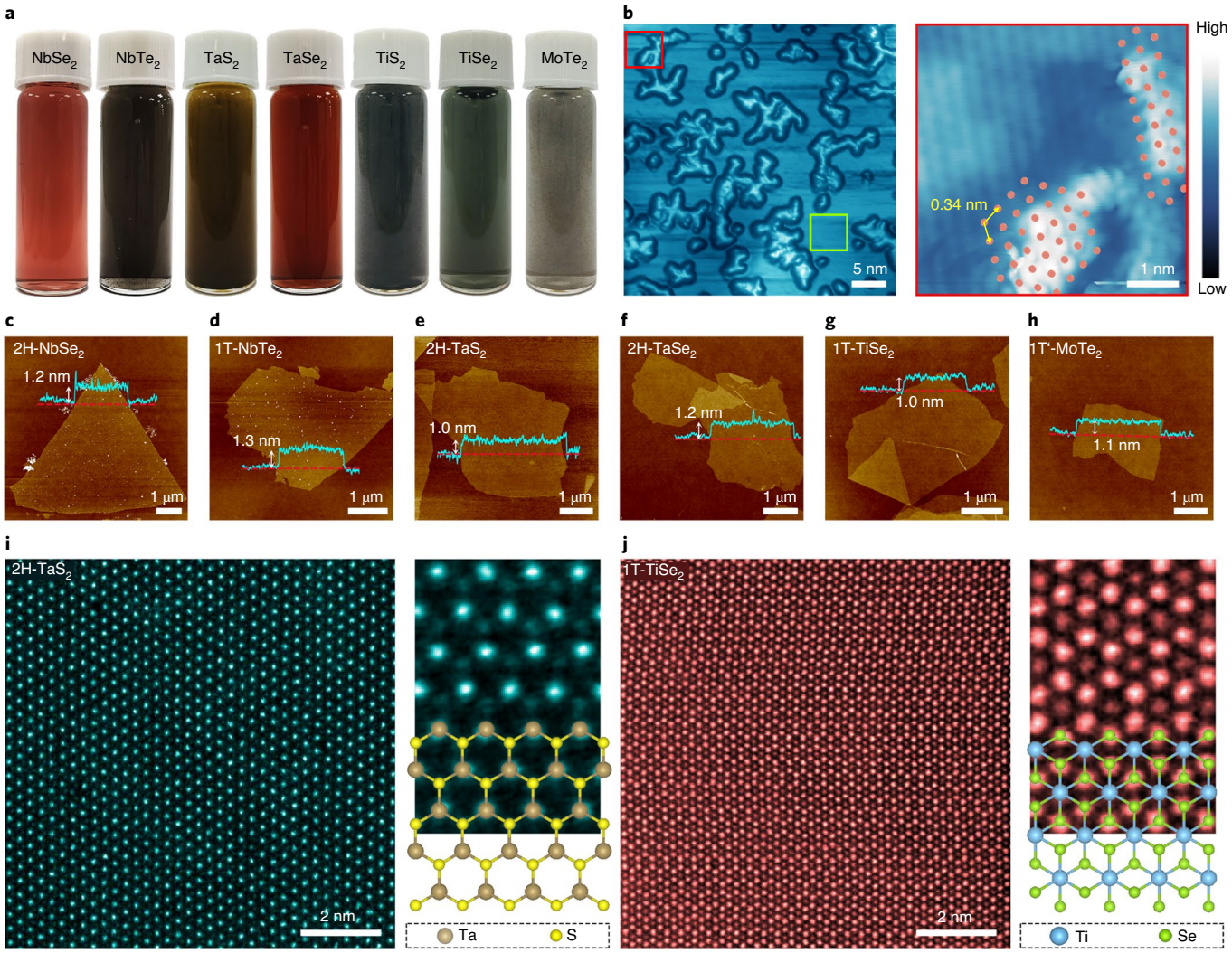

Fig. 1 | A general synthesis of 2D superconducting monolayers via cathodic exfoliation. a, Photographs of a series of TBA-exfoliated 2DSCs dispersed in PC solvent. The corresponding ultraviolet–visible spectra are presented in Supplementary Fig. 10. **b**, Large-area (left image) and magnified-view (right image, from the area labelled with a red square) STM imaging of TBA-intercalated $NbSe_2$. The orange dots denote the $NbSe_2$ lattice, with a lattice constant of 0.34 nm. The lattice for the area labelled by the green square can be seen in Supplementary Fig. 2b. Tunnelling parameter: −2.2 V, 10 pA (large-area image); −0.15 V, 80 pA (magnified-view image). **c–h**, AFM images and height profiles of 2H-$NbSe_2$ (**c**), 1T-$NbTe_2$ (**d**), 2H-TaS_2 (**e**), 2H-$TaSe_2$ (**f**), 1T-$TiSe_2$ (**g**) and 1T'-$MoTe_2$ (**h**) monolayers using TBA cations as electrochemical intercalant. **i,j**, Atomic-resolution STEM–ADF images of as-exfoliated 2H-TaS_2 (**i**) and 1T-$TiSe_2$ (**j**) monolayer. The close-up STEM–ADF image with the corresponding atomic model is presented in the right panels. Scale bars, 5 nm (**b**, left image), 1 nm (**b**, right image), 1 μm (**c–h**, AFM images) and 2 nm (**i,j**, STEM images).

a cathodic intercalant towards the production of a wide range of high-quality monolayer 2DSCs, including Nb(Se/Te)$_2$, Ta(S/Se)$_2$, Ti(S/Se)$_2$ and $MoTe_2$ (refs. [4,10,26,27]) and their one-step incorporation into basic vdWHs. Figure 1 illustrates the cathodic exfoliation of layered bulk TMDs into monolayer and few-layer 2DSCs using tetrabutyl ammonium (TBA) cations. TBA (0.05 M) dissolved in propylene carbonate (PC) was used to demonstrate cathodic exfoliation of more than seven types of bulk TMD materials. Upon applying a voltage of −5 V, these layered materials show rapid volumetric expansion and exfoliation into thin flakes (Fig. 1a). To better understand the crystallinity of the intercalated materials, we performed scanning tunnelling microscopy (STM) imaging of the TBA-intercalated 2DSCs drop-cast onto the SiO_2/Si substrate with prepatterned Au electrodes (Supplementary Fig. 2). The large-scale STM image (Fig. 1b) reveals bright protrusions randomly scattered over the whole flake. At a low sample bias, we managed to resolve the intact atomic lattice in both the flat and protrusion regions (Supplementary Fig. 2b). This suggests that the bright features are associated with uniformly intercalated molecules buried under the $NbSe_2$ surface layer, which can be rinsed off with solvent under sonication, as is supported by the STM images in Supplementary Fig. 20. Seven prototypical 2DSCs materials, including Nb(Se/Te)$_2$, Ta(S/Se)$_2$, Ti(S/Se)$_2$ and $MoTe_2$, were cathodically exfoliated, which demonstrates the generality of this method for the synthesis of 2DSCs.

The thickness and crystallinity of the as-exfoliated flakes were analysed to further evaluate the exfoliation efficiency of 2DSCs, as given in Supplementary Figs. 3–9. Figure 1c–h shows the atomic force microscopy (AFM) images and line profiles of the as-exfoliated 2DSC monolayers. We note that all the layered TMD materials show fast expansion and exfoliation behaviours but with a slightly different statistical thickness distribution, which presumably can be attributed to the different interlayer bonding strength between all these TMDs. We can readily achieve a yield (>80%) of 1–5 layers of 2DSC thin films, as evidenced by a statistical analysis of

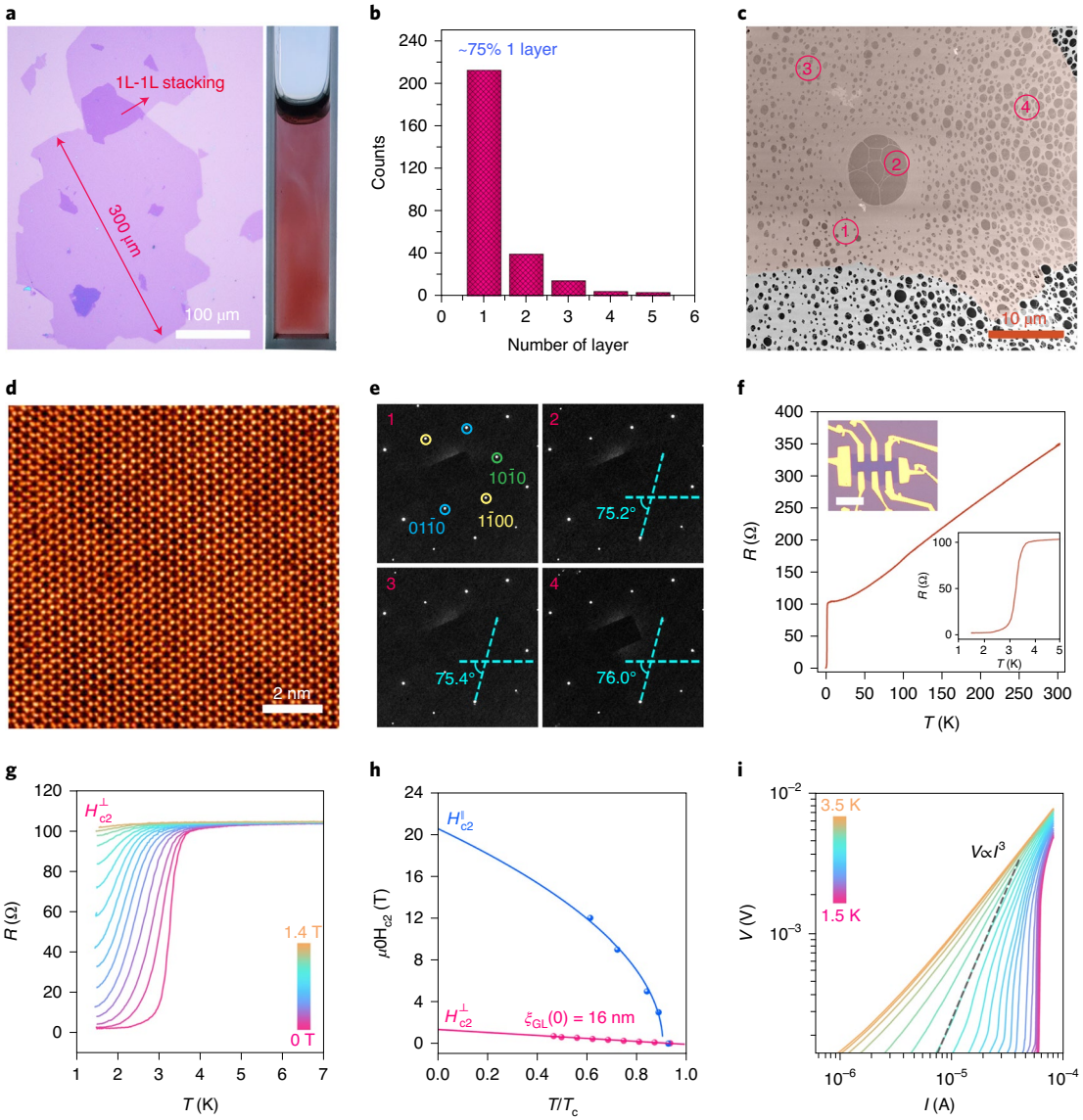

Fig. 2 | Structural and superconductivity characterization of highly crystalline $NbSe_2$ monolayer. a, Optical microscopic image of a representative large-sized $NbSe_2$ monolayer (~300 μm). Right inset: digital photograph of TPA-exfoliated $NbSe_2$ flakes in PC. **b**, Histogram of the thickness distribution of as-exfoliated $NbSe_2$ flakes. **c**, SEM image of as-exfoliated $NbSe_2$ flake (highlighted in false colour) drop-cast onto a TEM grid. The zoomed-in SEM image is shown in Supplementary Fig. 21. **d**, Atomically resolved STEM–ADF image shows the intact lattice of the $NbSe_2$ monolayer. **e**, The corresponding SAED patterns are acquired from various regions marked in panel **c**. The angle between the [01$\bar{1}$0] direction and the horizontal axis is indicated in each panel. **f**, Temperature-dependent longitudinal resistance (R_{xx}) for a monolayer $NbSe_2$ device. Upper inset: optical microscopic image of a typical monolayer $NbSe_2$ Hall bar device. Lower inset: resistance detail from 1.5 to 7 K. **g**, Temperature-dependent R_{xx} of a monolayer $NbSe_2$ device under different perpendicular magnetic fields ranging from 0 to 1.4 T. **h**, Temperature-dependent upper critical field H_{c2} under out-of-plane ($H_\perp$) and in-plane ($H_\parallel$) magnetic fields. Solid lines: fitting based on Ginzburg–Landau theory. **i**, Voltage–current (V–I) characteristics at different temperatures on a logarithmic scale. Dashed line indicates the expected $V \propto I^3$ behaviour at the BKT transition. Scale bars, 100 μm (**a**), 10 μm (**c**), 2 nm (**d**) and 20 μm (**f**).

multiple AFM images (Supplementary Figs. 3–9). Scanning tunnelling electron microscopy (STEM) imaging was then conducted to assess the density of atomic defects of the as-exfoliated flakes. Large-view STEM images of monolayer TaS_2 (Fig. 1i) and $TiSe_2$ (Fig. 1j) flakes reveal a nearly perfect atomic lattice with a very low defect density. The high crystallinity of all the other 2DSC monolayers was also confirmed by STEM images, as shown in Supplementary Figs. 3–9. Our STEM results reveal that the crystallinity of the exfoliated 2DSC monolayers is superior that of monolayer flakes grown by MBE[8] and CVD[17] methods.

We now focus on $NbSe_2$ (refs. [8,10,28]), a prototypical 2D superconductor, as a model system to carry out a systematic investigation of the exfoliation efficiency and crystallinity of thin flakes, as well as of their superconducting properties. When a dilute electrolyte consisting of 150 ppm tetrapropyl ammonium (TPA) cation in PC solvent is used (Supplementary Figs. 11–15), a small portion of large-sized single-crystal monolayer $NbSe_2$ (up to 300 μm) can be acquired via a direct detachment from the cathode. Note that this is larger than the monolayer $NbSe_2$ flake obtained by CVD and mechanical exfoliation[17]. TPA-intercalated $NbSe_2$ laminates (Supplementary Fig. 16) can be readily exfoliated into monolayer[3] (>75% yield) and few-layer flakes dispersed in a wide range of solvents via mild sonication for 30 s (Supplementary Figs. 17–20). These large-sized monolayer flakes were further deposited onto a carbon grid for

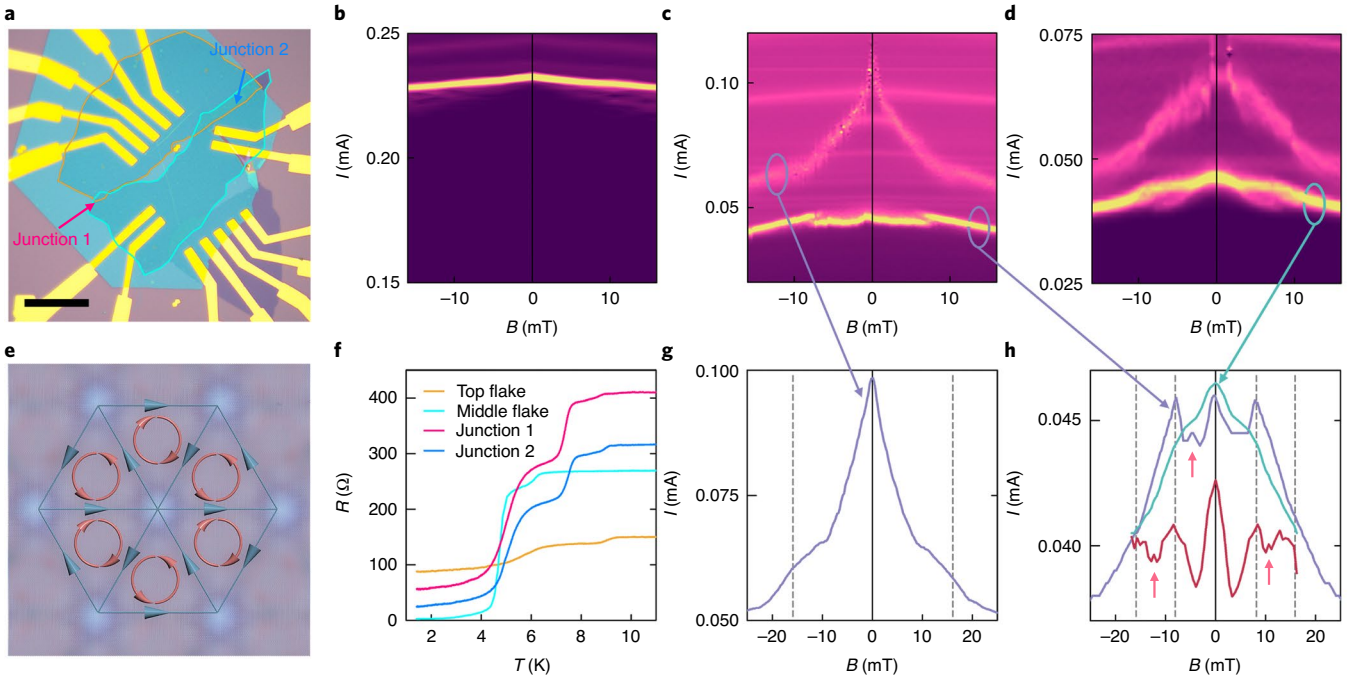

Fig. 3 | Josephson junction arrays in van der Waals heterostructures based on electrochemically exfoliated $NbSe_2$. **a**, Optical microscopic image of one twisted $NbSe_2$ device. The cyan border line marks a three-layer-thick $NbSe_2$ flake and the orange border line marks a two-layer-thick $NbSe_2$ flake. The overlapping regions of the two flakes form two Josephson junction arrays. Gold contacts were deposited on the $NbSe_2$ flake and then the device was covered with hexagonal boron nitride (green region). Scale bar, 20 μm. **b**, Differential resistance of the middle flake (marked by cyan in **a**) versus current and magnetic field. Superconductivity transition is conspicuous here and the critical current has a linear dependence on the magnetic field. Colour scale from purple to yellow: 0–3 kΩ. **c**, Differential resistance measured when the current is sent from the top flake (marked by orange in **a**) to the middle flake (marked by cyan in **a**) versus current and magnetic field. Superconductivity transitions associated with junction 1 and 2 are visible here and have oscillatory dependence on the magnetic field. Colour scale from purple to yellow: 0–600 Ω. **d**, Same as **c** but for a different configuration of the contacts. **e**, Schematic of the vortex configuration for the case of half flux quanta per moiré unit cell. The arrow indicates the direction of supercurrent flow. Current flow will form a closed loop in one triangle with the adjacent triangle having the opposite vortex. **f**, Resistance across two flakes and two junctions is measured with the temperature going down. The superconducting transition appears in all four parts. **g**, Dependence of the critical current of junction 1 as a function of magnetic field. Extracted from **c**. **h**, Dependence of the critical current of junction 2 as a function of magnetic field for different contact configurations (the purple curve is extracted from **c** and the green curve from **d**). For clarity, the parabolic background was subtracted from the green curve, resulting in the red curve. Grey lines are equidistant and mark the position of the peaks. Red arrows mark peaks observed at half-integer values of the frustration fraction. Measurements in **b**–**d**,**g**,**h** were done at 1.3 K.

transmission electron microscopy (TEM) and STEM characterization (Supplementary Fig. 21). The large-view STEM–annular dark field (STEM–ADF) image (Fig. 2d) of the $NbSe_2$ flake reveals long-range, periodic, bright (Se_2) and dim (Nb) dots arranged in the honeycomb lattice, with an atomic defect density lower than that of the monolayer grown by the CVD method (Supplementary Fig. 22)[17]. Selective area electron diffraction (SAED) was performed to probe the crystallinity of the exfoliated flakes (Fig. 2e). Grain boundaries or disorders are absent in all the flakes studied, as verified by observation of the same diffraction pattern with nearly identical orientation (±1.0°) for several randomly chosen regions (Fig. 2c), which further confirms that the exfoliated monolayer is a single crystalline flake.

As-exfoliated $NbSe_2$ flakes were patterned into a Hall bar geometry with Cr/Au electrodes using e-beam lithography for low-temperature transport measurements. Figure 2f shows the temperature dependence of the longitudinal resistance (R_{xx}) for a representative monolayer $NbSe_2$ flake at zero magnetic field. The residual resistance ratio (RRR), defined as the ratio between resistance at 300 K (R_{300K}) and resistance at the normal-state resistance above the transition temperature (R_{7K} in this case), is an indicator of crystal quality[17]. Strong scattering from impurities and defects leads to a large residual resistance and thus a small RRR[1]. The as-exfoliated $NbSe_2$ monolayer reveals an RRR of 3.5, which is smaller than that of mechanically exfoliated $NbSe_2$ (~10)[10] but larger than that of CVD-grown $NbSe_2$ (<2)[17], suggesting a low density of defect/disorder in the exfoliated $NbSe_2$ monolayer. A negligible defect/disorder in the $NbSe_2$ monolayer also results in a low resistance (~200 Ω per square) at 7 K, well below the $h/4e^2 \approx 6{,}450\,\Omega$ that is associated with the disorder-induced superconductor–insulator transition[14,29].

The superconducting transition temperature (T_c) of the exfoliated $NbSe_2$ monolayer is determined to be ~3.2 K. Note that T_c was defined as the temperature where resistance drops to half of the normal-state resistance (R_{7K}). Similarly, the upper critical field (H_{c2}) at finite temperature is defined as the field corresponding to half of R_{7K}. Figure 2g and Supplementary Fig. 24 show the temperature-dependent R_{xx} under out-of-plane ($H_\perp$) and in-plane ($H_\parallel$) magnetic field, respectively. The monolayer $NbSe_2$ exhibits a strong anisotropy in the superconductivity under the parallel ($H_\parallel$) and perpendicular ($H_\perp$) magnetic fields. Figure 2h shows the H_{c2}–T_c phase diagram for both $H_\perp$ and $H_\parallel$. A linear correlation between temperature and $H_{c2}^{\perp}$, can be modelled by the 2D Ginzburg–Landau (GL) theory[10,28]:

$$H_{c2}(T) = \frac{\Phi_0}{2\pi\xi_{GL}^2(0)}\left(1 - \frac{T}{T_c}\right) \quad (1)$$

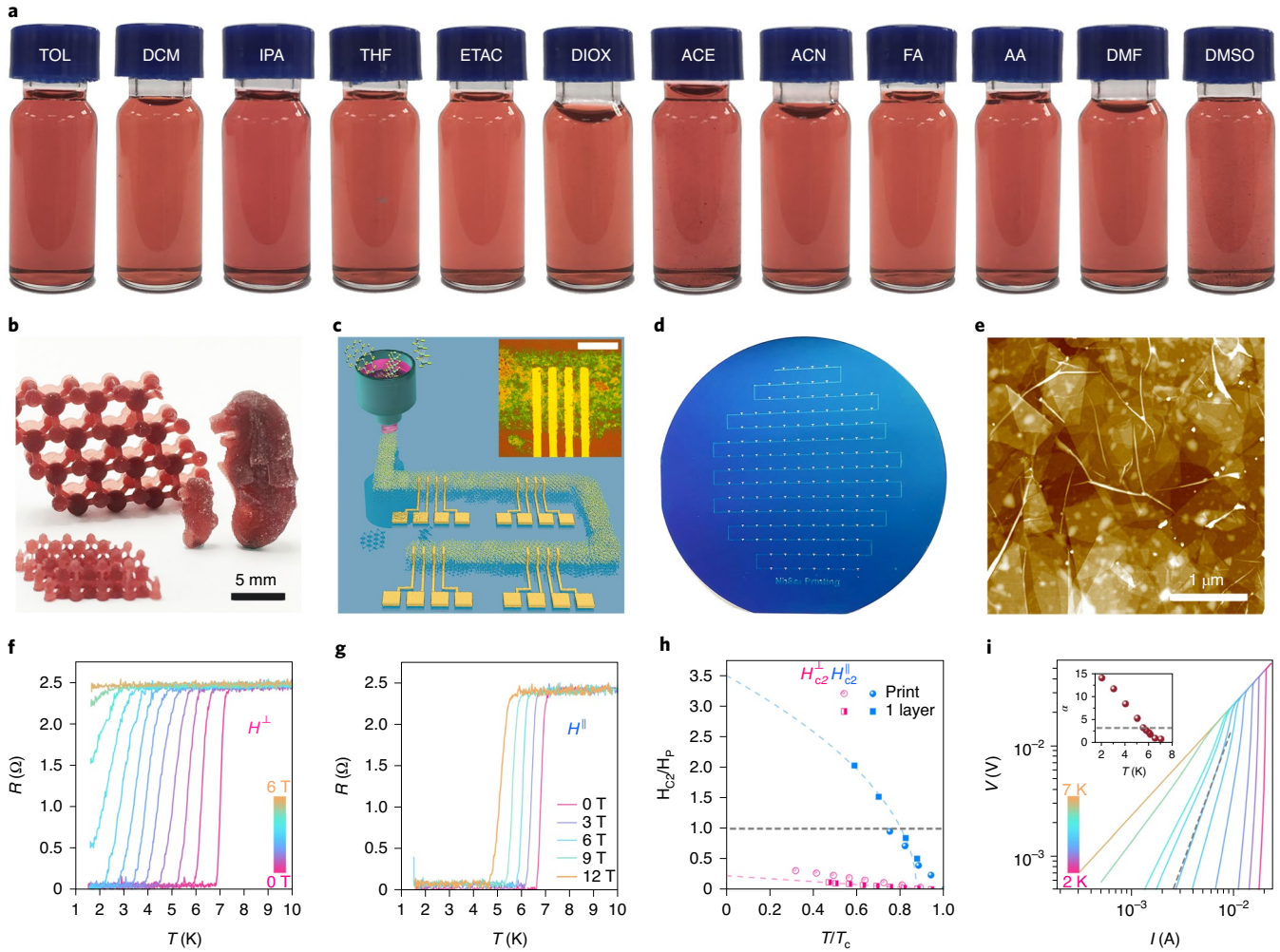

Fig. 4 | Printing the exfoliated $NbSe_2$ flakes. a, Dispersion of exfoliated $NbSe_2$ flakes in a diversity of solvents. Note: the full names and polarity indices for these solvents are provided in Supplementary Table 1. **b**, Digital photographs of $NbSe_2$ atomic models and Merlion statues fabricated by 3D printing. **c**–**e**, Schematic illustration (inset: optical microscopic image) (**c**), digital photograph (**d**) and AFM morphology (**e**) of an inkjet-printed large-area superconducting $NbSe_2$ wire on a 4-inch SiO_2/Si wafer. **f**–**i**, 2D superconductivity of printed $NbSe_2$ film. **f**,**g**, Temperature-dependent longitudinal resistance (R_{xx}) of a printed $NbSe_2$ film under different out-of-plane ($H_\perp$) (**f**) and in-plane ($H_\parallel$) (**g**) magnetic fields. **h**, The critical field H_{c2}/H_P as a function of transition temperature T_c/T_{c0} for printed $NbSe_2$ film under out-of-plane ($H_\perp$) and in-plane ($H_\parallel$) magnetic fields. The critical field H_{c2} and the critical temperature T_c are normalized by the BCS Pauli paramagnetic limit H_P and T_{c0}, respectively, for comparison. **i**, Voltage–current (V–I) characteristics at different temperatures on a logarithmic scale. Dashed line indicates the expected $V \propto I^3$ behaviour at the BKT transition. Scale bars, 5 mm (**b**), 100 μm (**c**), 1 μm (**e**).

where $\xi_{GL}(0)$ is the zero-temperature GL in-plane coherence length and Φ_0 is the magnetic flux quantum. A fitting of experimental data ($H_{c2}^{\perp}$–T_c) to equation (1) yields an in-plane coherence length of $\xi_{GL}(0) = 16$ nm, which is larger than the sample thickness (~1 nm) by a factor of 16. Such a long coherence length indicates a strongly suppressed depairing of the orbital magnetic effect associated with $H_\parallel$ in line with the characteristics of 2D superconductivity[10]. It is noted that $H_{c2}^{\parallel}$ is greatly enhanced, which goes beyond the Pauli paramagnetic limit ($H_P \approx 1.84 T_c$). Such an observation is consistent with the Ising superconductivity protected by Ising spin–orbit coupling[10,30]. Current excitation measurements (Fig. 2i) show that the V–I curve evolves from a linear to a power-law dependence ($V \propto I^\alpha$), which is in good agreement with the Berezinskii–Kosterlitz–Thouless (BKT) model for 2D superconductors. The BKT transition temperature (T_{BKT}) is determined to be 2.9 K at the temperature-dependent exponent $\alpha = 3$ (Supplementary Fig. 25). All the transport data confirm that large-sized as-exfoliated monolayer $NbSe_2$ behaves as a 2D Ising superconductor with a high crystallinity comparable with that of mechanically exfoliated flakes[10].

The majority of monolayer TMD superconductors are intrinsically air sensitive, posing a formidable challenge for their real applications[1,6,31]. Typically, a protection layer[32,33] or sample preparation in an inert environment[10] is required for device fabrication and characterization of 2DSC monolayers. In contrast, 2DSC monolayer suspensions show a notably enhanced stability and processibility, which permits sample processing in ways that would otherwise be difficult or impossible (Supplementary Fig. 26). In our case, solvent protection prevents the air degradation of vulnerable 2DSC monolayers in the solution phase, which allows synthesis and sample processing under ambient conditions.

This property also helps enormously in the fabrication of vdWHs and their devices (refer to Supplementary Figs. 27 and 28). Generally, fabrication of 3D stacks of air-sensitive 2D crystals is a very challenging task, which has to be undertaken in gloveboxes or vacuum chambers within a short period of time[6,32]. In contrast, the protective properties of the solvent notably enhance the lifetime of the flakes under ambient conditions[34,35]. At the same time, the self-cleaning properties of the 2D crystals[36] efficiently remove the

residual solvent, leaving the interface very clean. To demonstrate these advantages of our preparation method, we fabricated twisted flakes of $NbSe_2$ and studied their transport properties.

The device was first prepared by drop-casting the TPA-exfoliated $NbSe_2$ flakes onto the surface of Si/SiO_2 (300 nm of oxide). We then selected the overlapping flakes and deposited Ti/Au (3 nm/80 nm) contacts on various parts of the sample using the standard lithography procedure. All manipulations of the sample were conducted under ambient conditions. The transport properties for one of our devices are presented in Fig. 3. The device consists of two overlapping flakes—the top flake (outlined with orange, two-layer thick) and the middle one (outlined with cyan, three-layer thick). The magnetic dependence of the differential resistance (dV/dI) and the temperature dependence of the resistance for a single flake resistance are presented in Fig. 3b,f. Note that the magnetic field dependence of the critical current for individual flakes is very weak in the field range presented.

Figure 3c,d presents the magnetic field dependence of the junction, where the current is directed from one flake to another. The critical current associated with the superconducting to normal transition for each flake can be seen. On the overlapping flakes the superconducting to normal transition has a strong oscillatory behaviour as a function of magnetic field. We attribute this transition to the superconducting/normal transition at the interface between the two flakes. Different junctions have different periods of oscillation. Thus, oscillations coming from junction 2 have a period of $B = 8$ mT, which can be converted to a specific area, A, as $A = \Phi_0/B$, where $\Phi_0 = h/(2e)$ is the superconducting magnetic flux quantum ($\Phi_0 \approx 2\,\text{mT}\,\mu\text{m}^{-2}$) resulting in $A = 0.25\,\mu\text{m}^2$. We associate this specific area with the formation of the moiré pattern at the interface between the two closely aligned flakes (Fig. 3e).

The observed behaviour of the critical current in the presence of the applied magnetic field is reminiscent of the effect of a magnetic field on a frustrated superconducting Josephson junction array with triangular symmetry[37]. The controlling parameter in this case is the so-called frustration fraction, which is defined as $f = BA/\Phi_0$, where A is the area of the moiré unit cell. For such arrays the critical current is periodic in Φ_0 (which we associate with the two large peaks in Fig. 3h at $B \approx \pm 8$ mT) and has extra peaks at special frustration factors due to the formation of crystal vortex lattices[38]. For the triangular lattice the strongest secondary peak occurs at $f = ½$ (ref. [39]). As shown in Fig. 3h, we possibly observe peaks at $B \approx -5$ mT, -12 mT and 12 mT corresponding to $f \approx -0.5$, -1.5 and 1.5, as expected. Hence, our results are consistent with the proposed picture that the moiré pattern between two slightly twisted crystals acts as a periodic Josephson junction array with the period of the moiré lattice (Fig. 3e). We estimate from the area of the total overlapping interface (~10 μm^2), that there are hundreds of moiré–Josephson junctions formed between crystals that are described in terms of a frustrated classical 2D X–Y model with triangular symmetry. (Supplementary Figs. 29–30).

Both individual thin flakes and the junction demonstrate superconductivity at low temperature, suggesting that the protective property of the solvent and the self-cleaning mechanism at the interface enable the survival of these flakes during the lengthy fabrication process without encapsulation support. This will open up an avenue of simplified fabrication of $NbSe_2$ devices, which will lead to exciting physics as observed in such materials. Moreover, the dispersion of monolayer $NbSe_2$ superconductors in solvents allows them to be in high compatibility with current thin-film fabrication and printing technologies[40,41]. As shown in Fig. 4a, TPA-intercalated $NbSe_2$ samples can be readily dispersed in various solvents with just a mild sonication (Supplementary Table 1). The prepared materials can then be used in ink formulation for both 3D and 2D printing technologies. As shown in Fig. 4b, we demonstrated that exfoliated $NbSe_2$ monolayers can be blended with commercial Genesis resin for 3D printing. $NbSe_2$ atomic layers can be uniformly dispersed in the 3D printed structures with controlled topologies (Supplementary Fig. 33). Temperature-dependent magnetization of 3D printed structures under a magnetic field of 200 Oe reveals a diamagnetic signal at ~6.8 K corresponding to the superconducting transition (Supplementary Fig. 33h), which confirms that the superconductivity of $NbSe_2$ thin flakes is retained in 3D printed structures. Figure 4c,d shows that wafer-scale $NbSe_2$ superconducting wires can be patterned on a 4-inch SiO_2 substrate using inkjet printing. The AFM image reveals a continuous film with relatively uniform in-plane stacking for the printed $NbSe_2$ flakes. Subsequently, an array of electrodes was deposited onto these printed atomic layers to evaluate their superconducting properties. Similar to $NbSe_2$ bulk[10], printed $NbSe_2$ film (~100 nm in thickness) shows an upper critical field $H_{c2}^{\perp} \approx 4.4$ T (Fig. 4f) and a linear $H_{c2}^{\perp}$–T_c dependence. However, the in-plane magnetic response of printed $NbSe_2$ film resembles that of the $NbSe_2$ monolayer, with an upper critical field $H_{c2}^{\parallel}$ far exceeding its BCS Pauli paramagnetic limit (H_P) (Fig. 4g), suggesting the 2D superconductivity nature of the printed $NbSe_2$ film[10]. The printed $NbSe_2$ film also exhibits a high transition temperature ($T_c \approx 6.8$ K) and high upper critical field ($H_{c2}^{\perp} \approx 4.4$ T, $H_{c2}^{\parallel} \sim \approx 29$ T at 0 K). In addition, individual restacked few-layer $NbSe_2$ flakes also reveal the coexistence of a bulk-like transition temperature ($T_c \approx 6.5$ K) and monolayer-like upper critical field ($H_{c2}^{\parallel} \approx 30$ T at 0 K) (Supplementary Fig. 36), presumably attributed to the formation of interlayer Josephson junctions with contribution from Pauli paramagnetism and spin–orbit scattering in 2D TMD superconductors[42].

Conclusion

In summary, we have successfully developed a universal and mild electrochemical exfoliation approach for the scalable production of a library of highly crystalline 2D superconducting monolayers in solution phase. The single-crystal domain size and crystallinity of the as-exfoliated 2DSC monolayers are comparable to (in some cases, even superior to) the monolayer flakes obtained by other methods, including CVD and MBE growth. Moreover, the 2DSC monolayer suspension shows a remarkably enhanced environmental stability and solution processability. These materials can be readily integrated with current 2D and 3D printing technologies for the fabrication of wafer-scale superconducting device arrays, which offer a huge technological potential beyond the reach of existing materials.

Online content

Any methods, additional references, Nature Research reporting summaries, source data, extended data, supplementary information, acknowledgements, peer review information; details of author contributions and competing interests; and statements of data and code availability are available at https://doi.org/10.1038/s41563-020-00831-1.

Received: 23 May 2020; Accepted: 15 September 2020;
Published online: 26 October 2020

References

1. Saito, Y., Nojima, T. & Iwasa, Y. Highly crystalline 2D superconductors. *Nat. Rev. Mater.* **2**, 16094 (2016).
2. Xu, X., Yao, W., Xiao, D. & Heinz, T. F. Spin and pseudospins in layered transition metal dichalcogenides. *Nat. Phys.* **10**, 343–350 (2014).
3. Xi, X. et al. Strongly enhanced charge-density-wave order in monolayer $NbSe_2$. *Nat. Nanotechnol.* **10**, 765–769 (2015).
4. Li, L. J. et al. Controlling many-body states by the electric-field effect in a two-dimensional material. *Nature* **529**, 185–189 (2015).
5. Qin, S., Kim, J., Niu, Q. & Shih, C.-K. Superconductivity at the two-dimensional limit. *Science* **324**, 1314–1317 (2009).
6. Geim, A. K. & Grigorieva, I. V. Van der Waals heterostructures. *Nature* **499**, 419–425 (2013).

7. Liu, Y. et al. Van der Waals heterostructures and devices. *Nat. Rev. Mater.* **1**, 16042 (2016).
8. Ugeda, M. M. et al. Characterization of collective ground states in single-layer $NbSe_2$. *Nat. Phys.* **12**, 92–97 (2015).
9. Joe, Y. I. et al. Emergence of charge density wave domain walls above the superconducting dome in 1*T*-$TiSe_2$. *Nat. Phys.* **10**, 421–425 (2014).
10. Xi, X. et al. Ising pairing in superconducting $NbSe_2$ atomic layers. *Nat. Phys.* **12**, 139–143 (2015).
11. Ge, J.-F. et al. Superconductivity above 100 K in single-layer FeSe films on doped $SrTiO_3$. *Nat. Mater.* **14**, 285–289 (2014).
12. Saito, Y., Kasahara, Y., Ye, J., Iwasa, Y. & Nojima, T. Metallic ground state in an ion-gated two-dimensional superconductor. *Science* **350**, 409–413 (2015).
13. Graybeal, J. M. & Beasley, M. R. Localization and interaction effects in ultrathin amorphous superconducting films. *Phys. Rev. B* **29**, 4167–4169 (1984).
14. Jaeger, H. M., Haviland, D. B., Orr, B. G. & Goldman, A. M. Onset of superconductivity in ultrathin granular metal films. *Phys. Rev. B* **40**, 182–196 (1989).
15. Hebard, A. F. & Paalanen, M. A. Magnetic-field-tuned superconductor-insulator transition in two-dimensional films. *Phys. Rev. Lett.* **65**, 927–930 (1990).
16. Zhou, J. et al. A library of atomically thin metal chalcogenides. *Nature* **556**, 355–359 (2018).
17. Wang, H. et al. High-quality monolayer superconductor $NbSe_2$ grown by chemical vapour deposition. *Nat. Commun.* **8**, 394 (2017).
18. Lin, H. et al. Growth of environmentally stable transition metal selenide films. *Nat. Mater.* **18**, 602–607 (2019).
19. Cai, X., Luo, Y., Liu, B. & Cheng, H.-M. Preparation of 2D material dispersions and their applications. *Chem. Soc. Rev.* **47**, 6224–6266 (2018).
20. Han, J. H., Kwak, M., Kim, Y. & Cheon, J. Recent advances in the solution-based preparation of two-dimensional layered transition metal chalcogenide nanostructures. *Chem. Rev.* **118**, 6151–6188 (2018).
21. Peng, J. et al. Very large-sized transition metal dichalcogenides monolayers from fast exfoliation by manual shaking. *J. Am. Chem. Soc.* **139**, 9019–9025 (2017).
22. Cullen, P. L. et al. Ionic solutions of two-dimensional materials. *Nat. Chem.* **9**, 244–249 (2017).
23. Lin, Z. et al. Solution-processable 2D semiconductors for high-performance large-area electronics. *Nature* **562**, 254–258 (2018).
24. Zeng, Z. et al. Single-layer semiconducting nanosheets: high-yield preparation and device fabrication. *Angew. Chem. Int. Ed. Engl.* **50**, 11093–11097 (2011).
25. Watts, M. C. et al. Production of phosphorene nanoribbons. *Nature* **568**, 216–220 (2019).
26. Chen, P. et al. Charge density wave transition in single-layer titanium diselenide. *Nat. Commun.* **6**, 8943 (2015).
27. Yu, Y. et al. Gate-tunable phase transitions in thin flakes of 1T-TaS_2. *Nat. Nanotechnol.* **10**, 270–276 (2015).
28. Tsen, A. W. et al. Nature of the quantum metal in a two-dimensional crystalline superconductor. *Nat. Phys.* **12**, 208–212 (2015).
29. Fiory, A. T. & Hebard, A. F. Electron mobility, conductivity, and superconductivity near the metal-insulator transition. *Phys. Rev. Lett.* **52**, 2057–2060 (1984).
30. Lu, J. M. et al. Evidence for two-dimensional Ising superconductivity in gated MoS_2. *Science* **350**, 1353–1357 (2015).
31. Li, Q., Zhou, Q., Shi, L., Chen, Q. & Wang, J. Recent advances in oxidation and degradation mechanisms of ultrathin 2D materials under ambient conditions and their passivation strategies. *J. Mater. Chem. A* **7**, 4291–4312 (2019).
32. Cao, Y. et al. Quality heterostructures from two-dimensional crystals unstable in air by their assembly in inert atmosphere. *Nano Lett.* **15**, 4914–4921 (2015).
33. Khestanova, E. et al. Unusual suppression of the superconducting energy gap and critical temperature in atomically thin $NbSe_2$. *Nano Lett.* **18**, 2623–2629 (2018).
34. Hanlon, D. et al. Liquid exfoliation of solvent-stabilized few-layer black phosphorus for applications beyond electronics. *Nat. Commun.* **6**, 8563 (2015).
35. Li, J. et al. Ultrafast electrochemical expansion of black phosphorus toward high-yield synthesis of few-layer phosphorene. *Chem. Mater.* **30**, 2742–2749 (2018).
36. Kretinin, A. et al. Electronic properties of graphene encapsulated with different two-dimensional atomic crystals. *Nano Lett.* **14**, 3270–3276 (2014).
37. Brown, R. & Garland, J. Effect of magnetic-field-induced frustration on the superconducting transition of proximity-coupled arrays. *Phys. Rev. B* **33**, 7827 (1986).
38. Teitel, S. & Jayaprakash, C. Josephson-junction arrays in transverse magnetic fields. *Phys. Rev. Lett.* **51**, 1999 (1983).
39. Shih, W. & Stroud, D. Two-dimensional superconducting arrays in a magnetic field: effects of lattice structures. *Phys. Rev. B* **32**, 158 (1985).
40. Bonaccorso, F., Bartolotta, A., Coleman, J. N. & Backes, C. 2D-crystal-based functional inks. *Adv. Mater.* **28**, 6136–6166 (2016).
41. Macdonald, E. et al. 3D printing for the rapid prototyping of structural electronics. *IEEE Access* **2**, 234–242 (2014).
42. Klemm, R. A., Luther, A. & Beasley, M. Theory of the upper critical field in layered superconductors. *Phys. Rev. B* **12**, 877 (1975).

Methods

Cathodic intercalation of layered materials with quaternary ammonium cations. Cathodic intercalation of layered TMDs in the quaternary ammonium cation-based electrolyte was carried out in a two-electrode system using an electrochemical workstation (CHI 760E)[35]. Typically, a bulk TMD crystal with the size of ~2 × 2 × 1 (length × width × thickness) mm^3 was fixed on a Pt clip as cathode, and a Pt wire served as the anode. For general exfoliation of 2DSCs, tetrabutyl ammonium tetrafluoroborate ($TBABF_4$) dissolved in PC with a concentration of 0.05 M was used as electrolyte. To exfoliate 2DSCs, a voltage of −5 V versus Pt wire was applied on the cathode for 30 min. Subsequently, the delaminated flakes from the electrode were subjected to bath sonication at 100 W for 30 s for further exfoliation. Large-sized 2DSCs were exfoliated in the optimized electrolyte containing 150 ppm TPA in PC (denoted as TPA-exfoliated sample). Note that other exfoliation parameters and procedures, including exfoliation voltage, duration and sonication conditions, remained the same as for the other exfoliation experiments using TBA. The monolayer yield was calculated on the basis of the ratio between the amount of 2DSC monolayer and the total amount of SC flakes detached from the electrode via a statistical analysis of multiple AFM images. All the solvents and ammonium salts were purchased from Sigma-Aldrich and used as received. The layered materials were bought from HQ Graphene and used as received.

$NbSe_2$ ink formulation for 2D inkjet printing. Bulk $NbSe_2$ samples with typical dimensions of 2 × 2 × 1 mm^3 were fixed on a Pt clip as cathode and a Pt wire as anode. A cathodic voltage of −5 V versus Pt wire was applied for 30 min in the electrolyte consisting of 150 ppm TPA dissolved in PC solvent. The TPA-intercalated $NbSe_2$ was collected by filtration and then redispersed in acetone via sonication at 100 W for 30 s to remove intercalated molecules. Exfoliated $NbSe_2$ flakes were separated from the solution via centrifugation at 12,000 r.p.m. for 20 min. Finally, exfoliated $NbSe_2$ flakes were redispersed in *N*,*N*-dimethylformamide solvent by sonication at 500 W for 5 min to form the printable ink (~0.01 mg ml^{-1}) (Supplementary Fig. 34). Filtration of $NbSe_2$ ink through a 2-μm filter membrane allowed removal of the large-size $NbSe_2$ flakes, which avoids possible clogging, thus achieving a relatively uniform printed film via inkjet printing. A Fujifilm Dimatix Materials Printer (DMP-2850) equipped with a 10-picolitre nozzle cartridge was used to print and pattern $NbSe_2$ inks into superconducting wires. An electrode array (Cr/Au (3/80 nm)) was patterned on the printed $NbSe_2$ wires using laser lithography (Microtech Laser Writer, LW405B).

$NbSe_2$ ink formulation for 3D printing. TPA-exfoliated $NbSe_2$ flakes were mixed with commercial Genesis resin (Tethon 3D) for ink formulation (1 wt% of $NbSe_2$). Digital light projector technology was used for printing 3D superconducting objects with the setting parameters as follows: light intensity (33.4 mW cm^{-2}), slice thickness (0.05 mm) and exposure time (5 s) in each slice.

Characterization. The morphology of exfoliated 2DSC flakes was characterized by scanning electron microscopy (SEM) (FEI Verios 460 operated at 2 kV and 100 pA), AFM (Bruker Multimode 8 in Ar glovebox and DIMENSION FastScan in air) and high-resolution transmission electron microscopy (FEI Titan 80–300 S/TEM operated at 200 kV). Raman spectroscopic measurements (WITec Alpha 300 R) were performed at room temperature with laser excitation at 532 nm and power of <300 μW. STEM–ADF was performed using an aberration-corrected JEOL-ARM200F, equipped with a cold field emission gun, operated at 60 and 80 kV for metal disulfide and metal diselenide, respectively. The convergence semi-angle of the probe was ≈30 mrad. STEM–ADF images of metal diselenide and metal disulfide were collected using a half-angle range from ≈81 to 280 mrad, and from ≈30 to 110 mrad, respectively. X-ray photoelectron spectroscopy was carried out with a SPECS XR-50 X-ray MgKα (1,253.7 eV) source. Hall bar devices were fabricated with a standard electron-beam lithography procedure combined with thermal evaporation for the patterning metal electrodes consisting of Cr/Au of 3/80 nm. Temperature-dependent resistance of Hall bar devices was measured in an Oxford Teslatron PT 12 cryostat. The magnetization of $NbSe_2$ powder or 3D printing structures was characterized using a SQUID (quantum design MPMS 3) magnetometer with a temperature range of 2–300 K and an applied field range of −5,000 to 5,000 Oe.

Data availability

The datasets generated during the current study are available from the corresponding author on request.

Acknowledgements

J.Lu acknowledges support from MOE grants (MOE2017-T2-1-056 and MOE2019-T2-2-044) and NRF-CRP Grant (NRFCRP16-2015-02). J.Li acknowledges support from the National Natural Science Foundation of China (21703143). J.D. thanks NRF-CRP16-2015-01 (R284-000-159-281) for support of the 3D printing work. J.H.T. acknowledges support from Agency for Science, Technology and Research (A*STAR) under grant no. 1527000014. This work was supported by the National Research Foundation of Singapore under its Medium-Sized Centre Programme.

Author contributions

J.Lu supervised the project. J.Li, K.S.N. and J.Lu conceived the research and wrote the paper. J.Li and Z.L. performed the cathodic intercalation and exfoliation experiment. P.S. and J.Li. fabricated the Hall bar and vdWHs device. P.S. carried out the low-temperature transport measurement of Hall bar devices and analysed the results. J.Z. and K.V. performed the low-temperature transport measurement of twisted $NbSe_2$ vdWH devices and analysed the results. X.Z. performed the STEM imaging of exfoliated layered sheets and analysis. Z.Q. assisted with the STM imaging of TBA- and TPA-intercalated $NbSe_2$ structures. Z.W. and L.L. fabricated and measured the twisted $NbSe_2$ devices from mechanically exfoliated $NbSe_2$. M.Z. performed inkjet printing of superconducting wires. Y.Z. and W.J. carried out the 3D printing. T.S.H. assisted with the superconductivity measurement of 2D and 3D printing structures. J.Li performed the TEM, AFM and Raman characterization. W.Y., X.H., P.L., H.X., H.Y., C.C., S.J.P., J.D., J.T. and A.H.C.N discussed and commented on the manuscript.

Competing interests

The authors declare no competing interests.

Additional information

Supplementary information is available for this paper at https://doi.org/10.1038/s41563-020-00831-1.

Correspondence and requests for materials should be addressed to K.S.N. or J.L.

Reprints and permissions information is available at www.nature.com/reprints.